remote sensing

MDPI

Letter

The 2014 Mw 6.1 Ludian Earthquake: The Application of RADARSAT-2 SAR Interferometry and GPS for this Conjugated Ruptured Event

Yufen Niu [1,2], Shuai Wang [3], Wu Zhu [1], Qin Zhang [1,*], Zhong Lu [2], Chaoying Zhao [1] and Wei Qu [1]

1 College of Geology Engineering and Geomatics, Chang'an University, Xi'an 710054, China; 2015026021@chd.edu.cn (Y.N.); zhuwu@chd.edu.cn (W.Z.); cyzhao@chd.edu.cn (C.Z.); quwei@chd.edu.cn (W.Q.)
2 Roy M. Huffington Department of Earth Sciences, Southern Methodist University, Dallas, TX 75205, USA; zhonglu@smu.edu
3 School of Geomatics Science and Technology, Nanjing Tech University, Nanjing 211816, China; shwang@njtech.edu.cn
* Correspondence: dczhangq@chd.edu.cn; Tel.: +86-29-8233-9261

Received: 28 November 2019; Accepted: 19 December 2019; Published: 27 December 2019

Abstract: Although the Zhaotong–Ludian fault is a seismically active zone located in the boundary between the Sichuan–Yunnan block and the South China block, it has not experienced a large earthquake greater than Mw 7 since at least 1700. On 3 August, 2014, an Mw 6.1 earthquake (the Ludian earthquake) ruptured the Zhaotong active belt in Ludian County, Yunnan province, China. This earthquake was the largest earthquake recorded in the region since 2000, and it provides us with a unique opportunity to study the active tectonics in the region. The analysis of the aftershocks showed that two conjugate faults could have been involved in the event. We first used Global Positioning System (GPS) data and C-band RADARSAT-2 imagery to map the coseismic surface deformation. We then inverted the derived coseismic deformation for the slip distribution based on the constructed conjugate fault model. Finally, the coulomb failure stress due to the Ludian earthquake was estimated to investigate the potential seismic hazards in this region. Our investigations showed that the Ludian earthquake was mainly a bilateral rupture event. The major slip of the main shock was located at depths of 0–5 km, which is close but does not superpose with the aftershocks that are mostly located at depths of 5–20 km. Interestingly, the seismic moment released by the aftershocks (6.9×10^{18} N·m) was greater than that of the main shock (2.6×10^{18} N·m). This evidence suggests that the accumulated elastic strain at depths of 0–20 km could have been fully released by the Ludian earthquake and its subsequent aftershocks. Furthermore, our analysis of the coulomb failure stress changes due to the main shock showed that the aftershocks could be the result of dynamic triggering rather than static triggering.

Keywords: Ludian earthquake; conjugate fault; interferometric synthetic aperture radar; slip distribution

1. Introduction

The northeastern Yunnan rift zone is a seismically active region, located along the western boundary of the Sichuan–Yunnan Block and the eastern margin of the Qinghai–Tibet Plateau. The crustal motion in this area is dominated by large-scale fan-shaped rotation, as revealed by the Global Positioning System (GPS) velocity field (Figure 1) [1]. There are many tectonically active faults in Yunnan, e.g.,

the Xianshui He fault, the Xiaojiang fault, the Zemu He fault, the Anjing He fault, the Ninghui fault, and the Zhaotong–Ludian fault (Figure 1).

The Zhaotong–Ludian fault is located in the southeastern margin of the Qinghai–Tibet Plateau (Figure 1). This fault is a dextral strike-slip fault [2] and is a part of the boundary zone between Sichuan and Yunnan provinces. The GPS velocity field shows that the regional deformation is significant and is mainly dominated by NW-oriented tectonic stress (Figure 1) [2–4]. Many moderate earthquakes, including the 2004 Mw 5.6 Ludian earthquake, the 2012 Yiliang Mw 5.7 earthquake, the 2014 Yongshan Mw 5.3 earthquake, and the 2014 Jinggu Mw 6.6 earthquake, have occurred in this belt and its nearby regions in the past 20 years. However, a large earthquake greater than Ms 7.0 has not been recorded in the Zhaotong–Ludian fault since at least 1700. What is more, the GPS deformation field also shows that the Zhaotong–Ludian fault and its neighboring Lianfeng fault have a certain degree of locking [2], indicating that the Zhaotong fault could have accumulated sufficient elastic energy to produce a large earthquake. The occurrence of the 2014 Ludian earthquake provides us with a great opportunity to study the active tectonics in the region.

On 3 August 2014, an Mw 6.1 earthquake occurred in Ludian County, Yunnan province, southwestern China (Figure 1; Table 1). This event was the largest earthquake in Yunnan since 2000, and caused over 600 fatalities and rendered tens of thousands of people homeless. The epicenter of the earthquake was located in the area where many secondary faults conjugate, including the Xiaohe fault, the Baogu Nao fault, the Longshu fault, and the Dayan Dong fault (Figure 2b). Although different magnitudes have been reported [5–14], the focal mechanism solutions determined by the United States Geological Survey (USGS), the Institute of Earthquake Forecasting (IEF), and the Global Centroid Moment Tensor (GCMT) Project all revealed a left-lateral strike-slip faulting mechanism (Table 1, Figure 1). This is to be expected, considering the dominant extensional tectonic setting. Some studies have proposed that the Zhaotong–Ludian fault was not the seismogenic fault of the 2014 Ludian earthquake, because it is a thrust and right-lateral strike-slip fault. However, the existence of high stress and low *b*-values (~0.8) [2] for the Zhaotong–Ludian fault suggest that there may be some correlation between the Ludian earthquake and the Zhaotong–Ludian fault.

Table 1. Focal mechanism solutions for the 2014 Ludian earthquake.

No.	Solution	Magnitude	Longitude (°E)	Latitude (°N)	Depth (km)	Np1 (Strike, Dip, Rake)	Np2 (Strike, Dip, Rake)
1	IES [1]	6.5 *	103.3	27.1	12	341°/82°/−4°	72°/86°/−172°
2	USGS [2]	6.2 **	103.409	27.189	12	338°/74°/−32°	77°/59°/−162°
3	GCMT [3]	6.2 **	103.5	27.06	14.4	340°/86°/−9°	71°/81°/−175°
4	Wang et al. [8–13]	6.5 *	103.354	27.109	15	-	-
5	Liu et al. [7]	6.2 **	-	-	11	167°/87°/6°	74°/84°/177°
6	Guo et al. [14]	6.1 **	-	-	14	160°/80°/−20°	254°/70°/−189°

[1] Institute of Earthquake Forecasting, China Earthquake Administration (CEA); [2] United States Geological Survey (USGS); [3] Global Centroid Moment Tensor (GCMT) Project; * Ms, surface wave magnitude; ** Mw, moment magnitude.

In this study, we first mapped the surface deformation due to the Ludian earthquake using GPS and interferometric synthetic aperture radar (InSAR) data. We then analyzed the distribution of the aftershocks to determine the ruptured fault and its geometry. The coseismic slip distribution was inverted based on the mapped coseismic deformation, and the constructed fault model was obtained using the steepest-descent method (SDM) [15]. Finally, we investigated how the elastic strain was partitioned during the earthquake and evaluated the potential seismic risk in the region.

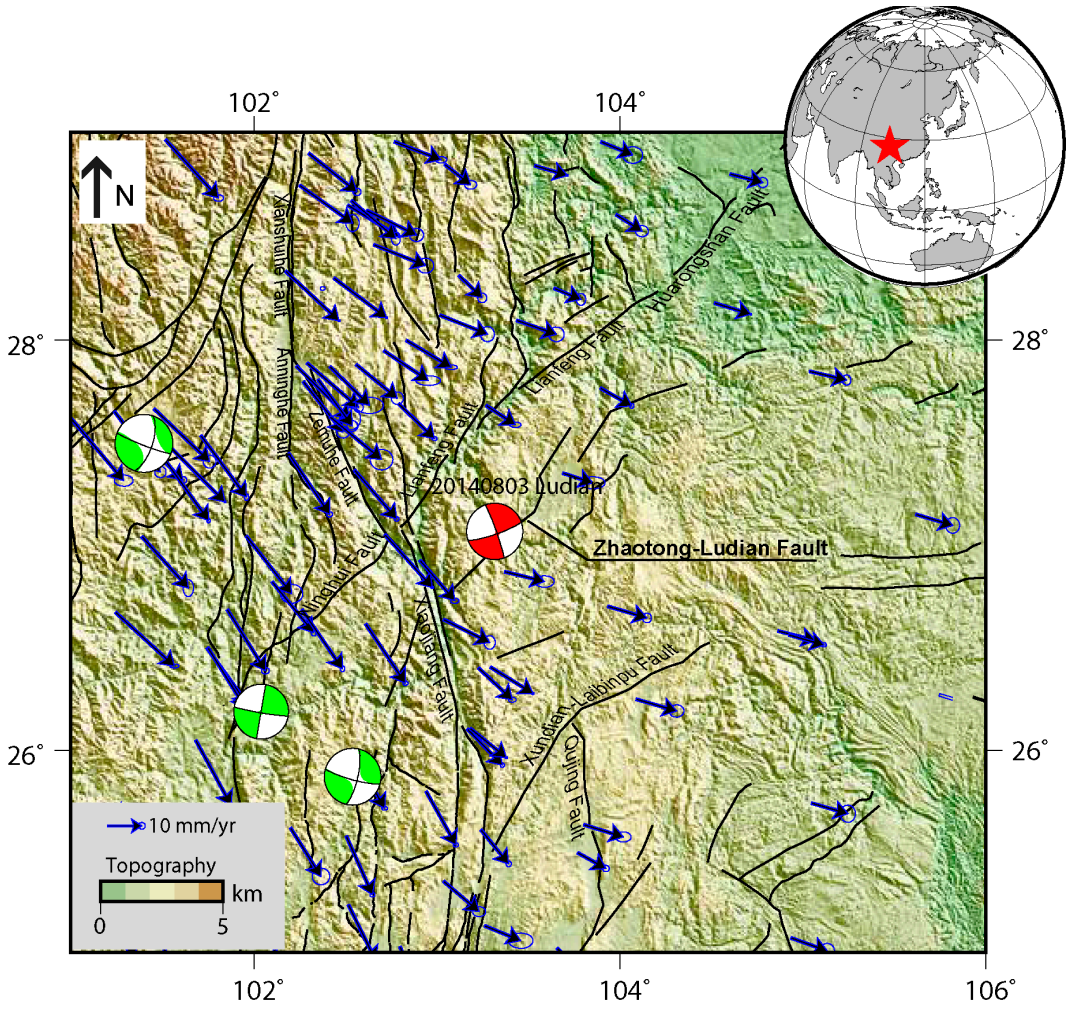

Figure 1. Tectonic setting of the study area. The red beach ball is the GCMT solution for the 2014 Ludian earthquake, and the green balls mark the locations of the Mw ≥ 6 historical earthquakes. The black lines are the regional active faults. The blue arrows are the crustal deformation from Zheng et al. [16].

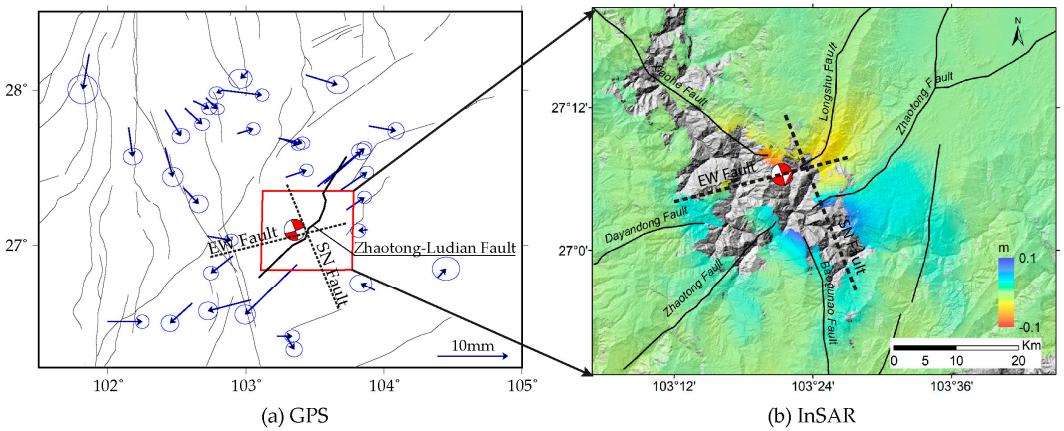

Figure 2. Coseismic deformation fields of the Ludian earthquake: (**a**) Coseismic horizontal displacements from the GPS measurements [17], with the red rectangle outlining the range of the 5-m resolution digital elevation model (DEM). (**b**) Coseismic line-of-sight (LOS) deformation field from the RADARSAT-2 data. The dashed lines in (**a**) and (**b**) indicate the inferred conjugate faults.

2. Observations

2.1. GPS Data and Analysis

The coseismic GPS data used in this study were provided by Wei et al. (2018) [17], consisting of data from 12 continuous GPS stations and 21 mobile GPS stations, which were remeasured after the earthquake. All the GPS stations are distributed within 200 km of the epicenter (Figure 2). The nearest station was about 26 km from the epicenter, and the farthest was 190 km.

We can see from Figure 2 that the coseismic deformation shows significant southward motion to the west of the Zhaotong–Ludian fault, whereas northward motion prevails to the east of the fault. This suggests that there were some left-lateral slip components during the earthquake, which is consistent with the focal mechanisms determined using seismic data. However, we note that the crust to the north of the epicenter tended to move eastward during the earthquake, as opposed to the crustal deformation to the south of the epicenter, which is dominated by westward motion. This deformation pattern is unlikely to have resulted from the left-lateral slip on the southwest-oriented Zhaotong–Ludian fault. Therefore, we propose that one more fault (oriented roughly to the W–E direction) may have formed a conjugate fault with the Zhaotong–Ludian fault, and could have been involved during the earthquake, to produce the deformation we analyzed.

2.2. InSAR Data and Analysis

As the GPS stations in this area are extremely sparse and located far from the epicenter, the finer features of the near-field coseismic displacement cannot be well captured. Fortunately, there are two SAR image scenes acquired before and after the earthquake by the RADARSAT-2 satellite (Figure 1), which allows us to image the near-field deformation and constrain the rupture kinematics.

The RADARSAT-2 synthetic aperture radar (SAR) images encompass the epicentral area and were acquired in ascending XF0W2 beam mode: Extra Fine Mode. Extra-Fine Resolution Beam Mode nominally provides a similar swath width and incidence angle coverage as the Wide Fine Beam Mode, at even finer resolutions [18,19]. The image acquisition dates were 4 March, 2014 and 16 April, 2015, respectively. The perpendicular baseline of this interferogram is 49 m, and the temporal baseline is 408 days.

We used GAMMA software to process the images under the framework of the two-pass InSAR approach (e.g., [20,21]). A digital elevation model (DEM) with a resolution of 5 m was used to remove the topographic phase from the interferogram. The coregistration procedure was conducted with the help of the DEM, which improved the coherence for the image pair [22]. The interferogram was multi-looked by a factor of 2 in range and 2 in azimuth (9 m × 9 m). We used the adaptive filter method to filter the interferogram and remove high-frequency noise. In addition, a quadratic ramp was estimated and removed from the interferogram by masking out the deforming area [23–25], to consider the orbital error. And the detailed process was shown in Figure S1.

The coseismic deformation derived from InSAR is shown in Figure 2b. In a broad sense, the InSAR coseismic deformation extends approximately 45 km in the E–W direction and about 40 km in the N–S direction. We can see that the near-field displacements are well mapped, except for the central high-relief mountainous areas, due to the earthquake-associated landslides [26–31], building damage [32], strong topographic relief, and/or saturation of the fringe rate. From the InSAR displacement field, the ground surface moved toward the sensor, with an approximate maximum of 10 cm in the southeast, and away from the sensor, with the same maximum of 10 cm in the northwest. However, what was the true direction of the coseismic displacement?

When combining the analysis of the GPS observations and the focal mechanism solutions, more specific conjugate faults are inferred in Figure 2b. Because the direction of the near S–N fault or the Xiaohe–Baogunao fault, which was likely the seismogenic fault inferred by many researchers, was almost parallel to the flight direction of the satellite, it was difficult to capture the horizontal displacements of the S–N fault. However, the movement of the inferred W–E fault was still acquired

from InSAR. As shown in Figure 2b, we can see that the north side of the W–E fault moved eastwards and the other side moved to the west, ignoring the small vertical component (a nearly pure strike-slip earthquake is suggested by many of the focal mechanism solutions). Therefore, the InSAR observations also provide more strong evidence for the existence of the E–W fault, i.e., the Ludian earthquake is highly likely to have been a conjugate rupture event.

3. Coseismic Deformation Modeling

Modeling coseismic displacement fields can provide new insights into the seismotectonic setting and seismic hazards of a tectonically active region. The analysis of the seismic waveforms [6], aftershock distributions [8–10], and apparent source time functions (ASTFs) [5] of the 2014 Ludian earthquake all suggest that the seismogenic structure of the earthquake was quite complex. The aftershocks distribute along the conjugate faults [8–10] and show a reverse L-shape. An analysis of the ASTFs also shows that two intersected faults could be responsible for the Ludian earthquake [5]. Zhang et al. [13] also concluded that the Ludian earthquake was a complex conjugated ruptured event. Therefore, in this study, we constructed a fault model consisting of two conjugate faults to shed light on the kinematics of the Ludian earthquake. Details of the constructed fault model are provided in the next section.

3.1. Fault Geometry

The critical displacement in the epicenter was lost due to the serious decorrelation of the InSAR data and the lack of near-field GPS stations, which brings challenges to determining the location of the causality fault from the geodetic data. In this study, we attempted to use the distribution of the aftershocks to determine the fault geometry.

The 961 aftershocks, relocated by Wang et al. [10] (Figure 3) using the double-difference location method, were used to help determine the fault geometry. We can see that the aftershock sequences are distributed dominantly in the SSE and EW directions, and clearly form an "L" shape. What is more, the aftershock sequences are vertically distributed at depth. These findings suggest that two steeply dipping faults, possibly forming a conjugate fault, were responsible for the Ludian earthquake (Figure 3).

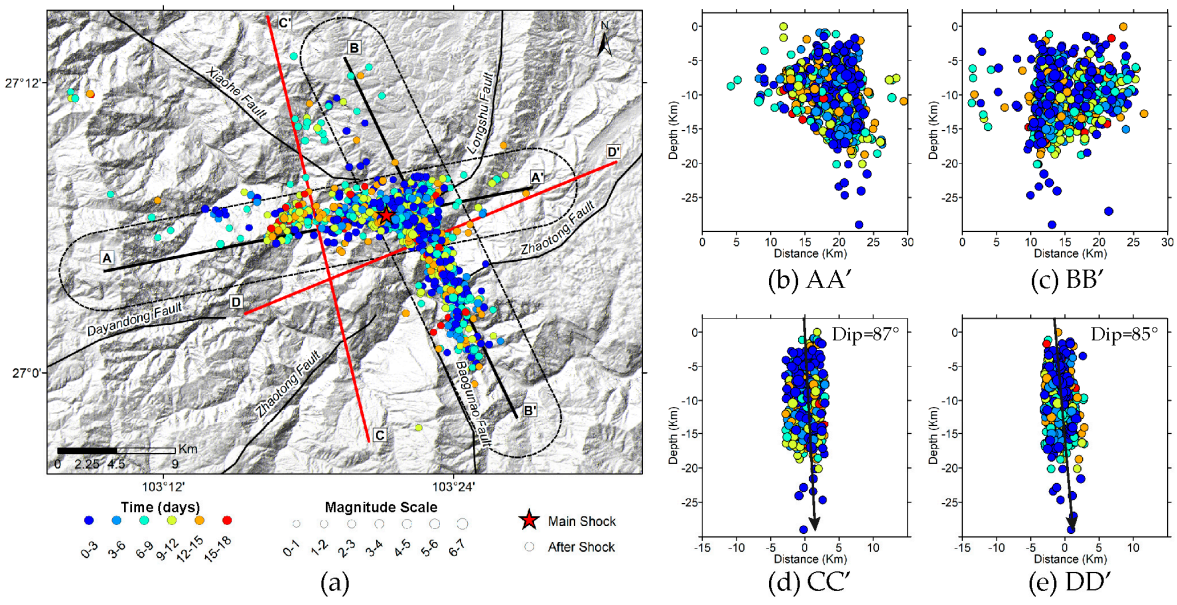

Figure 3. (**a**) Distribution of the relocated aftershocks. (**b**) Focal depth distribution of the aftershock sequences along the AA′ profile. (**c**)–(**e**) Same as (**b**), but along the BB′, CC′, and DD′ profiles, respectively.

We directly determined the seismogenic faults from the relocated aftershock distribution (Figure 3a), which consist of a roughly E–W oriented fault (hereafter F1) and a roughly S–N oriented fault (hereafter F2). The dip angles of the two faults were also calculated by the linear fit of the aftershocks in the vertical direction (Figure 3c,d). The widths and lengths of the two faults were enlarged along the strike and downdip directions (Figure 3). Detailed parameters of the two faults are listed in Table 2.

Table 2. Geometric parameters of the fault model.

No.	Direction	Strike (°)	Dip Angle (°)	Width (km)	Length (km)
F1	NNW–SSE (AA′)	337	87	30	30
F2	ENE–WSW (BB′)	81	85	30	30

3.2. Coseismic Slip Distributions

We used the SDM [15] to perform the inversion process. A layered Earth model from CRUST1.0 [33] was set up to model the crustal structure. Based on the fault geometry determined in Section 3.1, the fault planes were discretized into 1 km × 1 km patches to resolve the slip distribution. During the inversion, the rake angles of F1 were constrained from 170° to 185°, and F2 was from −20° to 20°, according to previous studies [9,13]. In order to account for the high spatial correlation of the pixels and to expedite the modeling process, we attempted to down-sample the InSAR data (Figure S2) using the quadtree method [23,34,35]. In addition, to overcome the problem of the non-uniqueness and instability of the inversion results, a smoothing constraint was applied to the slip distribution. An optimal smoothing factor was determined by analyzing the trade-off curve between data misfit and slip roughness, and a value of 0.11 was ultimately selected in this study (Figure S3). Figure 4 shows the final predictions and fitting residuals, with the predicted horizontal and vertical displacements shown in Figure 5. And Figure 6 shows the optimal slip model determined in this study.

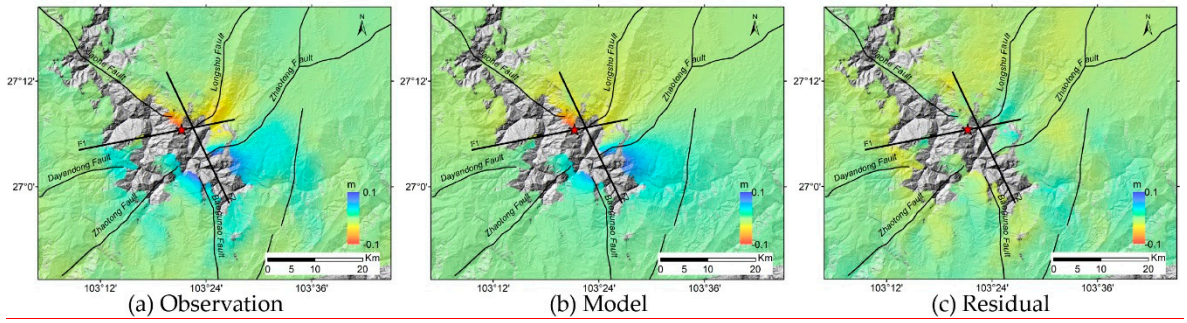

Figure 4. Coseismic displacement (negative indicates range displacement away from the satellite) and model for the distribution slip inversion of the 2014 Ludian earthquake: (**a**) the observed line-of-sight (LOS) displacements for the interval from 4 March, 2014 to 16 April, 2015; (**b**) the synthetic LOS displacement; and (**c**) the residual displacement.

We can see from Figure 4 that the predictions from the optimal slip model fit well with the observed InSAR and GPS, and the root-mean-square (RMS) misfits are 1.2 cm and 0.2 cm, respectively. The correlation coefficient between the observations and the prediction is 97.1%. In addition, to further verify the reliability of the inversion, we calculated the 3D deformation to compare with the results of the field survey after the event. As shown in Figure 5, the area with severe deformation is concentrated in regions A (F1) and B, and especially region B (F2). According to the field survey [26,31], most of the landsides triggered by the earthquake were distributed in regions A and B. Furthermore, in region B, the field investigation showed that the left plate was uplifted by about 0.3 m relative to the right plane [26], which is very similar to our result of 0.34 m.

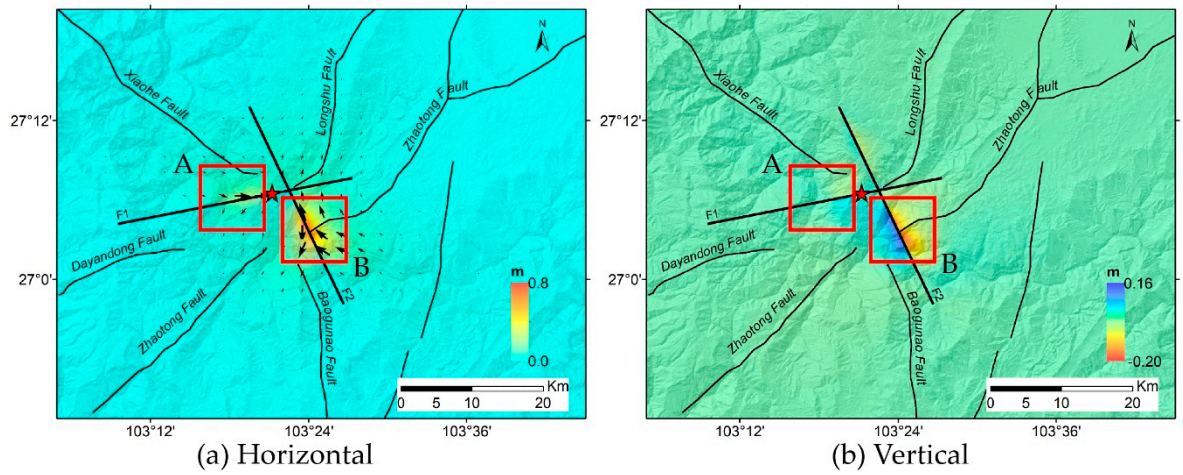

Figure 5. Predicted 3D displacement. (**a**) The horizontal surface displacement. (**b**) The vertical displacement. Regions A and B are the largest surface deformation areas for F1 and F2, respectively.

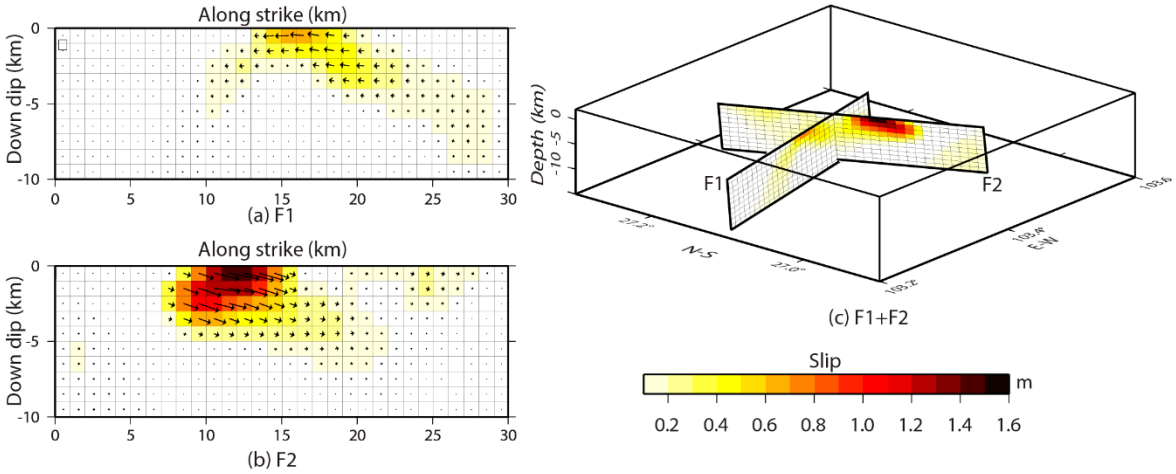

Figure 6. The optimal slip distribution for the 2014 Ludian earthquake inverted from the conjugate fault model. Slip distributions resolved (**a**) on F1 and (**b**) on F2. The black arrows show the movement direction of the hanging wall. (**c**) 3D visualization of the coseismic slip distribution.

As shown in Figure 6, we can see that the significant slips on F1 and F2 are both concentrated at shallow depths of 0–5 km, but there are some differences. F2 is dominated by left-lateral fault slip, which reaches up to 1.6 m. In contrast, the slip on F1 is characterized by right-lateral strike slip, with a maximum of 0.7 m. The seismic moment released by the fault slip on F2 was 1.9×10^{18} N·m (73% of the total), which was 2.5-times greater than that released on F1(0.7×10^{18} N·m, 27% of the total). This suggests that the Ludian earthquake was a predominately left-lateral strike-slip mechanism, which is consistent with the focal mechanism solution determined by the IEF, the USGS, and the GCMT Project. The total optimal slip model yielded a geodetic moment of 2.6×10^{18} N·m, corresponding to an Mw 6.2 event, assuming a shear modulus of 30 GPa, which is comparable to that estimated from the seismological data (Table 1). The comparable seismic moment magnitudes determined from the geodetic modeling and seismic data demonstrate that the postseismic deformation was likely very limited within the eight months following the earthquake.

4. Discussion

4.1. Comparison With Previous Studies

Similar to the conclusions of this study, most of the seismic models have demonstrated that the slips were mainly concentrated on the F2 or approximately F2 fault plane [13,36], and the released seismic moment was 62% on F2 and 38% on F1 [13], although differences exist in the slip magnitude and range. Based on the regional broadband seismograms, Liu et al. [36] showed that the F2 fault released most of the moment magnitude, the location of the maximum slip momentum was on the F2 fault (about 8 km to the south of the epicenter), the main slip occurred at a shallower depth (~3 km), and the fault ruptured to the surface. Zhang et al. [13] also acquired the slip distributions on both F1 and F2 by the use of more data sets, including local seismic data (strong motion and broadband) and teleseismic data. They showed that the range of the slip distribution was more concentrated and that the magnitudes were larger than those of Liu et al. [36] The results obtained in this study are more consistent with those of Zhang et al. [13], but there are some differences. The impacted area identified in this study was smaller than that of Zhang et al. [13], and the depth was shallower on both of the faults (F1: range ~7 km, depth 0–5 km; F2: range 17 km, depth, 0–8 km). The magnitudes of both faults in this study were also about three times those of Zhang et al. [13] These differences may have been caused by two factors. The first was the longer interval between the two SAR images, so that the aftershock deformation was included in the inverted deformation map, thus leading to a larger slip magnitude. The other was the near-field constraint by the near-field InSAR deformation map, which can improve the accuracy of the inversion.

In addition, Wei et al. [17] also inverted the 33 far-field GPS sites for slip distribution on two conjugate rectangular planes, and found that the slip patches were mainly concentrated on the northern part of the plane, which was approximately the F2 fault in our study. Although the misfit of GPS was 2.2 mm in the E–W direction and 1.8 mm in the S–N direction in their study, which is similar to our results (0.2 mm in both directions), the slip magnitude of F2 (0.15 m) was much less than our results and those of Zhang et al. [13] and Liu et al. [36], and the range (30 km) and depth (−18 to 0 km) [17] were much larger. Furthermore, the main surface rupture zones were not clearly shown in their slip distribution. This suggests that the inversion may not be reliable in the absence of near-field data sets. The addition of the InSAR-constrained observations significantly optimizes the results of the slip distribution, which makes the results more reasonable and finer. This implies that it was necessary to integrate InSAR observations for an in-depth study of the Ludian earthquake.

4.2. Coulomb Static Stress Change

Coseismic slip due to earthquakes can alter the stress states of neighboring faults, as well as the seismicity, via the transfer of stress. To evaluate the effect of the Ludian earthquake on the surrounding tectonic activities and the occurrence of aftershocks, we calculated the static coulomb failure stress (CFS) changes on the optimally oriented strike faults using the inverted best-fitting slip model. The friction coefficient was assumed to be 0.4, and the shear modulus was assumed to be 30 GPa. The regional tectonic principal stress, which is required for the estimation of the optimal failure directions, was simply assumed to be 100 bars, with an orientation of S45°E [37].

The CFS estimation shows that the CFS was greatly increased at shallow depths of 0–5 km (Figure 7). The Xiaohe and Longshu faults tend to be a high seismic risk due to the enhanced CFS along these two faults. Notably, we can see from Figure 7c,d that most of the aftershocks were located in regions that show a decreased CFS, indicating that these aftershocks were likely to have been triggered by dynamic stress rather than static stress transfer [38]. The seismic moment released by the aftershocks was approximately 6.9×10^{18} N·m greater than that released by the main shock (2.6×10^{18} N·m). What is more, the main slip region was located at depths of 0–5 km (Figure 6), which is spatially complementary with the depths of the aftershocks, which were mostly located at depths of 5–20 km (Figure 7c,d). These findings suggest that the elastic strain accumulated in the interseismic

cycle in the seismogenic region could have been fully released by the main shock and the subsequent aftershocks. As shown in Figure 2b, many faults conjugate in the epicentral zone of the Ludian earthquake. The absence of coseismic rupture on the deeper fractures (5–20 km) may therefore indicate that the deep structure of the region is extremely complex. At depth (5–20 km), structural barriers could have been formed at the intersection of the sub-faults to prevent the earthquake from fracturing into deeper parts. The elastic strain of the deeper parts could have been partitioned by the aftershocks, which suggests that the seismogenic depths of the Zhaotong–Ludian fault could be 0–20 km.

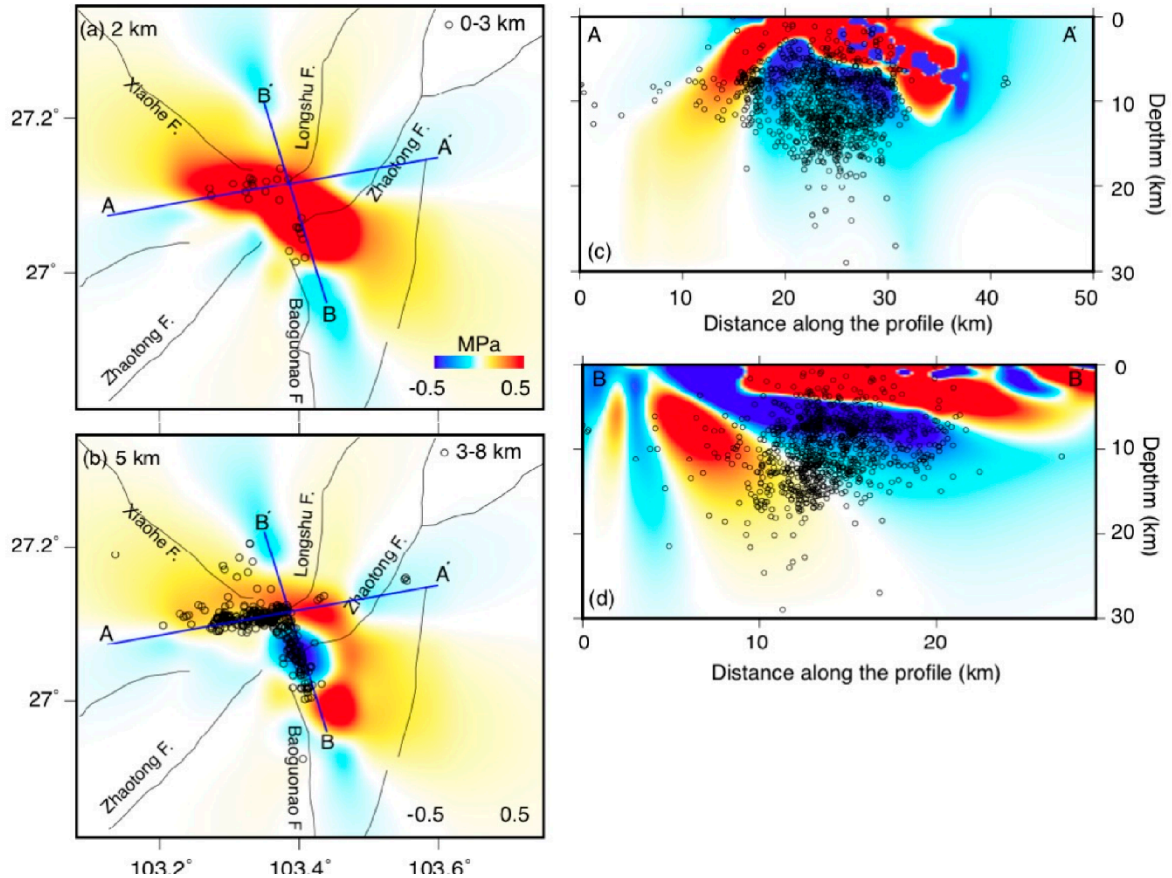

Figure 7. Coulomb failure stress changes on optimally oriented strike-slip faults at depths of (**a**) 2 km and (**b**) 5 km. (**c**)–(**d**) The coulomb failure stress changes along the profiles A-A′ and B-B′ shown in (**a**), respectively. The open black circles are the aftershocks. Note that the friction coefficient was chosen to be 0.4, and all the panels share the same color code.

5. Conclusions

In this study, we used GPS and InSAR, plus relocated aftershock data, to study the 2014 Ludian earthquake. InSAR provided an important near-field constraint on the detailed slip distribution inversion. The earthquake showed a complex deformation pattern, and a conjugate fault was deemed to be responsible for its occurrence. The major slip of the main shock was located at depths of 0–5 km, which is spatially complementary with the depth of the aftershocks, which were mostly located at depths of 5–20 km. The accumulated elastic strain at depths of 0–20 km could have been fully released by the Ludian earthquake and its subsequent aftershocks. Furthermore, the aftershocks could have been the result of dynamic triggering rather than static triggering.

Supplementary Materials: The following are available online at http://www.mdpi.com/2072-4292/12/1/99/s1. Figure S1: The detailed process for removing the orbital error. Figure S2: Quadtree decomposition image of coseismic deformation map. Figure S3: Trade-off curve between misfit and model roughness.

Author Contributions: All of the authors participated in the editing and reviewing of the manuscript. Y.N. led the research and processed the InSAR data. S.W. calculated the Coulomb stress change data. Y.N. and S.W. inverted the coseismic slip distribution. Q.Z., W.Z., Z.L., C.Z., and W.Q. analyzed and interpreted the results, and reviewed the manuscript. All authors contributed to the writing of this manuscript. All authors have read and agreed to the published version of the manuscript.

Funding: This research was funded by Chang'an university (Xi'an, China) through the Natural Science Foundation of China (NSFC) (nos. 41790445, 41731066, 41674001, 41874005, 41929001, 41901286, 41504005), the Fundamental Research Funds for the Central Universities (nos. 310826171005, 300102269207), the Chinese Postdoctoral Science Foundation (2016M602741), the Natural Science Basic Research Plan in Shaanxi Province of China (nos. 2018JQ4031, 2019JM-202), the Key Laboratory of Surveying and Mapping Science and Geospatial Information Technology of Ministry of Natural Resources (no. 201906) and the Shaanxi Postdoctoral Science Foundation (no. 2017BSHEDZZ20).

Acknowledgments: The authors would like to thank Lingyun Li, Ming Zhang for their meaningful suggestions. The DEM was provided by the Information Institute of Photogrammetry and Remote Sensing of Yunnan Province, China. Coseismic displacements of the GPS were provided by Wenxin Wei from the Institute of Earthquake Forecasting of the China Earthquake Administration (CEA). The aftershock data sets were provided by Weilai Wang from the Institute of Geophysics, CEA. The SDM program was provided by Rongjiang Wang.

Conflicts of Interest: The authors declare no conflict of interest.

References

1. Xu, X.W.; Wen, X.; Zheng, R.; Ma, W.; Song, F.; Yu, G. Pattern of latest tectonic motion and its dynamics for active blocks in Sichuan-Yunnan region, China. *Sci. China Ser. D Earth Sci.* **2003**, *46*, 210–226.
2. Wen, X.Z.; Du, F.; Yi, G.X.; Long, F.; Fan, J.; Yang, P.X.; Xiong, R.W.; Liu, X.X.; Liu, Q. Earthquake potential of the Zhaotong and Lianfeng fault zones of the eastern Sichuan-Yunnan border region. *Chin. J. Geophys.* **2013**, *56*, 3361–3372.
3. Kan, R.J.; Zhang, S.C.; Yan, L.S.; Yu, F.T. Present Tectonic Stress Field and Its Relation to the Characteristics of Recent Tectonic Activity in Southwestern China. *Chin. J. Sin.* **1977**, *2*, 96–109.
4. Kan, R.; Wang, S.; Huang, K.; Sung, W. Modern tectonic stress field and relative motion of intraplate block in Southwestern China. *Seismol. Geol.* **1983**, *5*, 79–90.
5. Xu, L.S.; Zhang, X.; Yan, C.; Li, C.L. Analysis of the Love waves for the source complexity of the Ludian M (s) 6.5 earthquake. *Chin. J. Geophys.* **2014**, *57*, 3006–3017.
6. Zhang, Y.; Xu, L.S.; Chen, Y.T.; Liu, R.F. Rupture process of the 3 August 2014 Ludian, Yunnan, M (w) 6.1 (M (s) 6.5) earthquake. *Chin. J. Geophys.* **2014**, *57*, 3052–3059.
7. Liu, C.; Xu, L.S.; Chen, Y.T. The 3 August 2014, Ms 6.5 Ludian Earthquake. Available online: http://www.cea-igp.ac.cn/tpxw/270724.html (accessed on 1 November 2018).
8. Fang, L.H.; Wu, J.P.; Wang, W.L.; Lü, Z.; Wang, C.; Yang, T.; Zhong, S. Relocation of the aftershock sequence of the Ms 6.5 Ludian earthquake and its seismogenic structure. *Seismol. Geol.* **2014**, *36*, 1173–1185.
9. Zhang, G.W.; Lei, J.S.; Liang, S.S.; Sun, C.Q. Relocations and focal mechanism solutions of the 3 August 2014 Ludian, Yunnan M (s) 6.5 earthquake sequence. *Chin. J. Geophys.* **2014**, *57*, 3018–3027.
10. Wang, W.L.; Wu, J.P.; Fang, L.H.; Lai, G.J. Double difference location of the Ludian M (s) 6.5 earthquake sequences in Yunnan province in 2014. *Chin. J. Geophys.* **2014**, *57*, 3042–3051.
11. Xu, X.W.; Jiang, G.Y.; Yu, G.H.; Wu, X.Y.; Zhang, J.G.; Li, X. Discussion on seismogenic fault of the Ludian M (s) 6.5 earthquake and its tectonic attribution. *Chin. J. Geophys.* **2014**, *57*, 3060–3068.
12. Cheng, J.; Wu, Z.; Liu, J.; Jiang, C.; Xu, X.; Fang, L.; Zhao, X.; Feng, W.; Liu, R.; Liang, J. Preliminary report on the 3 August 2014, M w 6.2/M s 6.5 Ludian, Yunnan–Sichuan border, southwest China, earthquake. *Seismol. Res. Lett.* **2015**, *86*, 750–763. [CrossRef]
13. Zhang, Y.; Chen, Y.T.; Xu, L.S.; Wei, X.; Jin, M.P.; Zhang, S. The 2014 M (w) 6.1 Ludian, Yunnan, earthquake: A complex conjugated ruptured earthquake. *Chin. J. Geophys.* **2015**, *58*, 153–162.
14. Guo, Z. Moment Tensor Solution of Ms6.5 2014 Ludian Earthquake. Available online: http://www.eq-igl.ac.cn/upload/files/2014/10/21112032347.pdf (accessed on 20 October 2018).
15. Wang, R.; Diao, F.; Hoechner, A. SDM-A Geodetic Inversion Code Incorporating with Layered Crust Structure and Curved Fault Geometry. In Proceedings of the EGU General Assembly Conference Abstracts, Vienna, Austria, 7–12 April 2013.

16. Zheng, G.; Wang, H.; Wright, T.J.; Lou, Y.; Zhang, R.; Zhang, W.; Shi, C.; Huang, J.; Wei, N. Crustal deformation in the India-Eurasia collision zone from 25 years of GPS measurements. *J. Geophys. Res. Solid Earth* **2017**, *122*, 9290–9312. [CrossRef]
17. Wei, W.X.; Jiang, Z.S.; Shao, D.S.; Shao, Z.G.; Liu, X.X.; Zou, Z.Y.; Wang, Y. Coseismic displacements from GPS and inversion analysis for the 2014 Ludian 6. 5 earthquake. *Chin. J. Geophys.* **2018**, *61*, 1258–1265.
18. Morena, L.; James, K.; Beck, J. An introduction to the RADARSAT-2 mission. *Can. J. Remote Sens.* **2004**, *30*, 221–234. [CrossRef]
19. Thompson, A.A.; Luscombe, A.; James, K.; Fox, P. Radarsat-2 Mission Status: Capabilities Demonstrated and Image Quality Achieved. In Proceedings of the 7th European Conference on Synthetic Aperture Radar, Friedrichshafen, Germany, 2–5 June 2008; pp. 1–4.
20. Rosen, P.A.; Hensley, S.; Joughin, I.R.; Li, F.K.; Madsen, S.N.; Rodriguez, E.; Goldstein, R.M. Synthetic aperture radar interferometry. *Proc. IEEE* **2000**, *88*, 333–382. [CrossRef]
21. Massonnet, D.; Rossi, M.; Carmona, C.; Adragna, F.; Peltzer, G.; Feigl, K.; Rabaute, T. The displacement field of the Landers earthquake mapped by radar interferometry. *Nature* **1993**, *364*, 138. [CrossRef]
22. Lu, Z.; Dzurisin, D. Ground surface deformation patterns, magma supply, and magma storage at Okmok volcano, Alaska, from InSAR analysis: 2. Coeruptive deflation, July–August 2008. *J. Geophys. Res. Solid Earth* **2010**, *115*. [CrossRef]
23. Ji, L.; Wang, Q.; Xu, J.; Ji, C. The July 11, 1995 Myanmar–China earthquake: A representative event in the bookshelf faulting system of southeastern Asia observed from JERS-1 SAR images. *Int. J. Appl. Earth Obs. Geoinf.* **2017**, *55*, 43–51. [CrossRef]
24. Lu, Z.; Dzurisin, D. InSAR imaging of Aleutian volcanoes. In *InSAR Imaging of Aleutian Volcanoes*; Springer: Chichester, UK, 2014; pp. 87–345. Available online: https://link.springer.com/chapter/10.1007/978-3-642-00348-6_6 (accessed on 15 October 2019).
25. Rosen, P.A.; Hensley, S.; Zebker, H.A.; Webb, F.H.; Fielding, E.J. Surface deformation and coherence measurements of Kilauea Volcano, Hawaii, from SIR-C radar interferometry. *J. Geophys. Res. Planets* **1996**, *101*, 23109–23125. [CrossRef]
26. Chen, X.; Hu, K.; Ge, Y.; Wang, Y. Surface ruptures and large-scale landslides caused by "8· 03" Ludian Earthquake in Yunnan, China. *Mt. Res.* **2015**, *1*, 65–71.
27. Chen, X.L.; Liu, C.G.; Wang, M.M.; Zhou, Q. Causes of unusual distribution of coseismic landslides triggered by the Mw 6.1 2014 Ludian, Yunnan, China earthquake. *J. Asian Earth Sci.* **2018**, *159*, 17–23. [CrossRef]
28. Shi, Z.; Xiong, X.; Peng, M.; Zhang, L.; Xiong, Y.; Chen, H.; Zhu, Y. Risk assessment and mitigation for the Hongshiyan landslide dam triggered by the 2014 Ludian earthquake in Yunnan, China. *Landslides* **2017**, *14*, 269–285. [CrossRef]
29. Xu, C. Utilizing coseismic landslides to analyze the source and rupturing process of the 2014 Ludian earthquake. *J. Eng. Geol.* **2015**, *23*, 755–759.
30. Xu, C.; Xu, X.W.; Shen, L.L.; Du, S.; Wu, S.; Tian, Y.; Li, X. Inventory of landslides triggered by the 2014 Ms 6.5 Ludian earthquake and its implications on several earthquake parameters. *Seism. Geol.* **2014**, *36*, 1186–1203.
31. Zhou, S.; Chen, G.; Fang, L. Distribution pattern of landslides triggered by the 2014 Ludian earthquake of China: Implications for regional threshold topography and the seismogenic fault identification. *ISPRS Int. J. Geo Inf.* **2016**, *5*, 46. [CrossRef]
32. Lin, X.; Zhang, H.; Chen, H.; Chen, H.; Lin, J. Field investigation on severely damaged aseismic buildings in 2014 Ludian earthquake. *Earthq. Eng. Eng. Vib.* **2015**, *14*, 169–176. [CrossRef]
33. Laske, G.; Masters, G.; Ma, Z.; Pasyanos, M. Update on CRUST1. 0—A 1-Degree Global Model of Earth's Crust. *Geophys. Res. Abstr.* **2013**, *15*, 2658.
34. Jónsson, S.; Zebker, H.; Segall, P.; Amelung, F. Fault slip distribution of the 1999 M w 7.1 Hector Mine, California, earthquake, estimated from satellite radar and GPS measurements. *Bull. Seismol. Soc. Am.* **2002**, *92*, 1377–1389.
35. Ji, L.; Wang, Q.; Xu, J.; Feng, J. The 1996 Mw 6.6 Lijiang earthquake: Application of JERS-1 SAR interferometry on a typical normal-faulting event in the northwestern Yunnan rift zone, SW China. *J. Asian Earth Sci.* **2017**, *146*, 221–232. [CrossRef]
36. Liu, C.L.; Zheng, Y.; Xiong, X.; Fu, R.; Shan, B.; Diao, F.Q. Rupture process of M (s) 6.5 Ludian earthquake constrained by regional broadband seismograms. *Chin. J. Geophys.* **2014**, *57*, 3028–3037.

37. Heidbach, O.; Rajabi, M.; Cui, X.; Fuchs, K.; Müller, B.; Reinecker, J.; Reiter, K.; Tingay, M.; Wenzel, F.; Xie, F. The World Stress Map database release 2016: Crustal stress pattern across scales. *Tectonophysics* **2018**, *744*, 484–498. [CrossRef]
38. Nissen, E.; Elliott, J.; Sloan, R.; Craig, T.; Funning, G.; Hutko, A.; Parsons, B.; Wright, T. Limitations of rupture forecasting exposed by instantaneously triggered earthquake doublet. *Nat. Geosci.* **2016**, *9*, 330. [CrossRef]